

High-Precision MRI-Compatible Force Sensor with Parallel Plate Structure

Takashi Tokuno¹, Mitsunori Tada² and Kazunori Umeda¹

¹ Course of Precision Engineering, School of Science and Engineering, Chuo University, Japan

² Digital Human Research Center, National Institute of Advanced Industrial Science and Technology, Japan

tokuno@sensor.mech.chuo-u.ac.jp

Abstract—This paper presents an MRI-compatible optical force sensor: its principle, structure and performance. Our force sensor employs an optical micrometry based on differential measure of light intensity. This technology enables highly accurate and sensitive two degrees-of-freedom displacement sensing by using a point source, a photo detector and an optical lens. The developed force sensor achieves MRI compatibility by placing all the electric and metallic components outside MRI, and connecting the light path between the optical components by using multi-core optical fibers. The sensor head component has parallel plate structure and is made of glass fiber reinforced poly-ether-ether-keton those help reducing axial interference and hysteresis characteristics of plastic resin. The accuracy of this force sensor is better than 1.6 %F.S. under the applied force ranging from 0 to 3 N.

I. INTRODUCTION

In recent years, magnetic resonance imaging (MRI) has been gaining popularity among many researchers. However, we cannot use standard mechanical and electrical devices composed of ferromagnetic materials and electrical circuits in the imaging area of MRI [1], since MRI requires homogeneous magnetic field and radio frequency (RF) pulse for inducing the nuclear magnetic resonance (NMR) during the imaging process.

The development of force sensor that do not interfere with MRI is one of the key technologies in experiments using MRI, especially for studies such as biomechanics, anatomy [2], brain function [3], rehabilitation [4] and MRI-guided surgery [5], [6], so that we can quantify the exerted force or the voluntary human movement simultaneously while scanning images. In this paper, we propose a simple, accurate and versatile MRI-compatible optical force sensor for the human function studies using MRI.

There have been several MRI-compatible force sensors in the past literature [7], [8], [9], [10]. Liu *et al.* have developed a grip dynamometer based on hydraulic pressure [7], while Hidler *et al.* have utilized a custom 6-axis non-magnetic load cell [10] in order to achieve MRI compatibility. In the former case, the grip force exerted to a hand grip device is transmitted to a pressure transducer outside the scanner room by a water-filled nylon tube. Hence it has a dead zone over a wide range of force, from 0 to 80 N due to the friction of a piston built into the hand grip device.

Among existing MRI-compatible force sensors optics based implementations [8], [9] offer a suitable combination

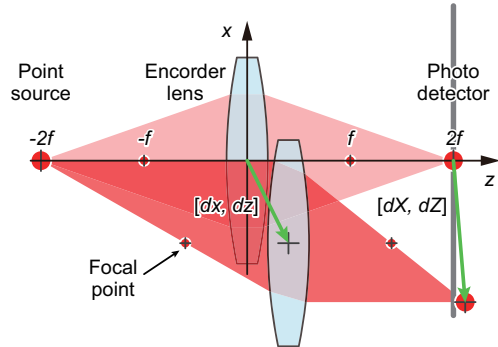


Fig. 1. Principle of the force sensor [9]

of simplicity and accuracy for our purpose. Tada and Kanade developed a uniaxial optical force sensor [9]. Their sensor achieves MRI compatibility by placing all the electric and metallic elements outside the scanner room and connecting a light path between optical elements by using optical fibers. The accuracy of the sensor under the application of multi-directional force was 3 %F.S. [11], since they did not consider axial interference of the sensor head structure: they employed a thin plate structure to convert the applied force into minute displacement.

This paper presents a uniaxial optical force sensor with redesigned sensor head structure taking account of the axial interference. We evaluate the accuracy of this force sensor under the application of multi-directional force to validate the performance of our sensor.

II. PRINCIPLE

A. Basic Idea: Optical Micrometry

Figure 1 illustrates the basic principle of our force sensor that Tada and Kanade have proposed [9]. The coordinate origin is placed at the position where an optical lens with focal length f , called an encoder lens, is at rest. A point source is positioned at $[0, -2f]^T$, while the center of an imaging plane at $[0, 2f]^T$. The imaging plane is perpendicular to the optical axis: hence the image of the point source is focused onto the center of the imaging plane when the encoder lens is at the origin.

A minute translational displacement of the encoder lens $[dx, dz]^T$ causes the position of the focused image to move

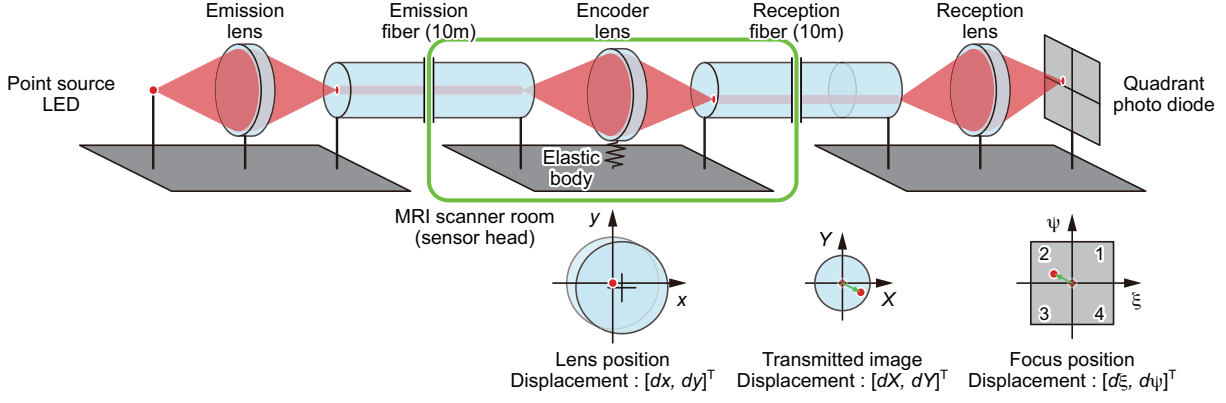


Fig. 2. Implementation of the optical micrometry

$[dX, dZ]^T$, where

$$[dX, dZ]^T = \left[2dx - \frac{dx dz}{f + dz}, \frac{dz^2}{f + dz} \right]^T. \quad (1)$$

Neglecting higher order terms,

$$[dX, dZ]^T = [2dx, 0]^T \quad (2)$$

is obtained.

The encoder lens has magnified x axial translation dx two times onto the change in the imaging plane, whereas nullifying the effect of z axial displacement. The shift of the focused image location within the imaging plane is measured with high accuracy by using a position detectable photo sensor, such as a photo diode or a position sensitive device (PSD).

The one-dimensional optical micrometry described above can be generalized to two-dimensional case, $[dX, dY, dZ]^T = [2dx, 2dy, 0]^T$, where lens displacement within the x - y plane perpendicular to the optical axis is measured by using a quadrant photo diode or a two-dimensional PSD.

In the MRI environment where ferromagnetic materials or electronic circuits are severely restricted, all the electric devices on the base component should be positioned apart from MRI. Such a configuration is realized by using multi-core optical fibers to connect a light path from the actual point source to the point source in Figure 1, and to connect the imaging plane in Figure 1 to the actual photo detector.

B. Implementation

Shown in Figure 2 is the schematic diagram of an actual implementation of our force sensor. We employed additional two optical lenses to connect the optical devices and the optical fibers transmitting the focused image position. Light signal emitted from the point-source red LED (VS679TM, Alpha-One Electronics Co., Japan) throws its image on the end face of the multi-core emission fiber (FU-77, Keyence Co., Japan) through the emission lens (W18-S0290-063-ABC, Nihon Sheet Glass Co., Japan).

The light emitted from the other end of the emission fiber is condensed again by the encoder lens (the same model

as the emission lens) and throws light distribution on the end face of the reception fiber (the same model as the emission fiber). The light distribution is transmitted through the reception fiber, and is finally focused onto the imaging plane of the quadrant photo diode (MI-1515H-4D, Moririka Co., Japan) through the reception lens (the same model as the emission lens). Both the emission and the reception optical fibers are 10 meters long and have 217 cores in diameter of 1.3 mm.

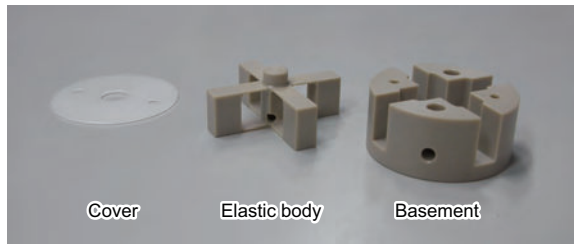
The encoder lens is mounted on an elastic body. As derived in equation (2), displacement of the encoder lens $[dx, dy]^T$ cause the focused image to move minutely $[dX, dY]^T$ on the end face of the reception fiber and $[d\xi, d\psi]^T$ on the imaging plane of the quadrant photo diode. Note that z axial displacement dz is omitted here, since the resulting focused image movement in this direction is negligible as long as the displacement is minute.

The output current from each segment of the photo diode is amplified with the I-V converter composed of an operational amplifier (OP400, Analog Devices Inc., USA). The output voltages from these four I-V converters are fed to instrumentation amplifiers (INA105, Texas Instruments Inc., USA), which compute:

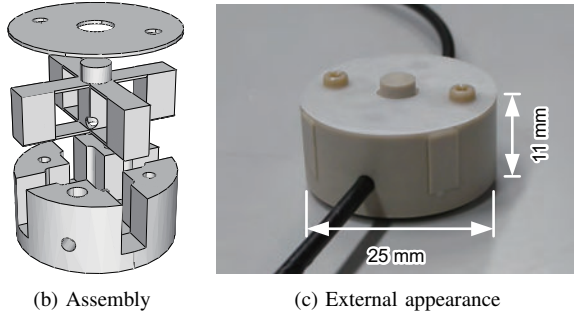
$$\begin{cases} V_\xi = (V_1 + V_4) - (V_2 + V_3) \\ V_\psi = (V_1 + V_2) - (V_3 + V_4), \end{cases} \quad (3)$$

where V_i ($i = 1, 2, 3, 4$) is the output voltages from the i -th I-V converter, while V_ξ and V_ψ are the differential voltage along ξ and ψ axis. Please refer to [11] for the detail of the signal conditioning.

As given in Equation (2), $[dx, dy]^T = \frac{1}{2}[dX, dY]^T$. Similarly, $[dX, dY]^T = \mathbf{R}[d\xi, d\psi]^T$, where \mathbf{R} is a 2×2 rotation matrix. This rotation matrix is necessary to align X - Y and ξ - ψ coordinates, since they are on different bases and are connected by an optical fiber. If the displacement of the focused image is sufficiently small, $d\xi$ and $d\psi$ are proportional to dV_ξ and dV_ψ , where dV_ξ and dV_ψ are the variation of the differential voltage. Thus, we finally obtain the relation between the lens displacement $[dx, dy]^T$ and variation of the differential voltage $[dV_\xi, dV_\psi]^T$ as



(a) Designed sensor head parts; cover, elastic body and base



(b) Assembly (c) External appearance

Fig. 3. Design of the sensor head component

$$[dx, dy]^T = \frac{1}{2} c \mathbf{R} [dV_\xi, dV_\psi]^T, \quad (4)$$

where c is a proportionality constant.

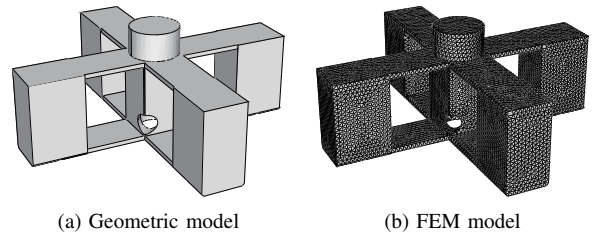
III. DESIGN OF THE SENSOR HEAD COMPONENT

A. Designing criteria

We designed the geometry of an elastic body with finite element simulation to get a rough idea of the rated force and rigidity ratio. The elastic body converts the applied force into displacement of the encoder lens. Since we are designing a uniaxial force sensor, the elastic body must have a directionality: deformable only in one direction so that we can achieve high axial independence (i.e. little axial interference). It should have a simple structure as well so that the machining process is simplified. There are several possible structures for an elastic body of a force sensor in the literature. Among them a parallel plate structure offers a suitable combination of directionality and simplicity for this purpose.

Figure 3-(a) illustrates designed sensor head. It has three components: a cover, an elastic body and a basement. The elastic body has four parallel plate structures supporting a vertical column where an encoder lens is placed at the bottom. The plates have the same dimensions: 5.6 mm in length, 3.8 mm in width and 0.4 mm in thickness. The other ends of the parallel plate structure and two multi-core optical fibers are bonded to the basement with an instant adhesive to ensure stability. The cover prevents disturbance light from coming into the optical path.

Figure 3-(b) and (c) shows the assembling process and the external appearance of our force sensor, respectively. The elastic body and the basement are made of glass



(a) Geometric model (b) FEM model

Fig. 4. Finite element model for numerical simulation

TABLE I
MATERIAL CONSTANTS FOR FINITE ELEMENT ANALYSIS

Constant name	Constant value
Young's modulus	$8.3 \times 10^3 \text{ N/mm}^2$
Poisson's ratio	2.8×10^{-1}
Density	$1.4 \times 10^{-3} \text{ g/mm}^3$

fiber reinforced poly-ether-ether-ketone (PEEK450GF, Nippon Polyenco Co., Japan) to reduce hysteresis characteristics of plastic resin, while the cover is made of polyacetal resin (Delrin, DuPont Co. Ltd., USA) to facilitate the machining process. The sensor head component has 25 mm in diameter, 11 mm in height and 6.5 g in weight.

B. Rigidity

Characteristics of the elastic body, rigidity and natural frequency, was evaluated by using finite element simulation. As shown in Figure 4, we created a finite element model of the elastic body from a three dimensional geometric model for this purpose. The model consists of 115327 tetrahedral elements that have material constants assigned as shown in Table I. During the analyses, four blocks at the end of the parallel plate structure are fixed in order to simulate the adherence of these region to the basement. We utilized a general purpose finite element analysis software (Abaqus 6.7, Dassault Systèmes Co., France) for this simulation.

Rigidity of the elastic body was estimated by applying point force of 3 N to its top, and computing the resulting deformation along the force direction. There were four force directions in this evaluation: a normal and three tangentials. The normal force is top-to-bottom direction of the model shown in Figure 4, thus the elastic body is expected to deform along this directional force. The tangential force are perpendicular to the normal direction. Table II illustrates the results of the analyses. The numbers at the end of the tangential conditions denote the angle of the applied tangential force with the optical axis. We only show the results for 0 to $\pi/2$ radian because of the symmetry of the elastic body.

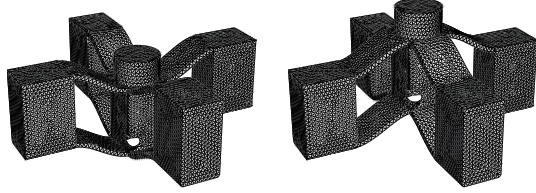
As can be seen in Table II, the rigidity of the elastic body in the normal direction is $2.1 \times 10^{-1} \text{ N}/\mu\text{m}$. As we expected the elastic body is more than 30 times more stiff in the tangential direction than in the normal direction.

C. Natural Frequency

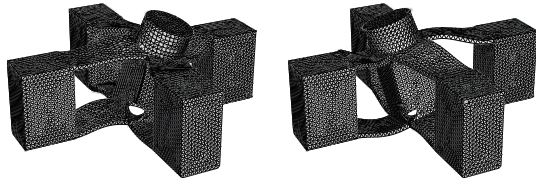
Natural frequency of the elastic body was determined by using the same simulation environment as that given in

TABLE II
DISPLACEMENT OF THE OPTICAL LENS UNDER THE APPLICATION OF
3 N FORCE IN FOUR DIRECTIONS

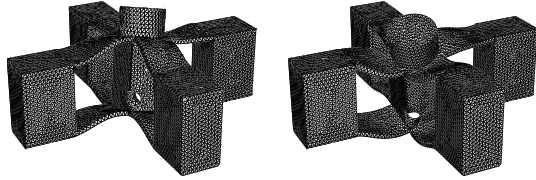
Direction	Displacement	Rigidity	Ratio
Normal	$1.5 \times 10^{-1} \mu\text{m}$	$2.1 \times 10^{-1} \text{ N}/\mu\text{m}$	NA
Tangential (0)	$4.9 \times 10^{-1} \mu\text{m}$	$6.1 \text{ N}/\mu\text{m}$	3.0×10
Tangential ($\pi/4$)	$3.9 \times 10^{-1} \mu\text{m}$	$7.7 \text{ N}/\mu\text{m}$	3.7×10
Tangential ($\pi/2$)	$2.1 \times 10^{-1} \mu\text{m}$	$1.4 \times 10 \text{ N}/\mu\text{m}$	7.0×10



(a) First mode: 4.7 kHz



(b) Second mode: 2.6×10 kHz



(c) Third mode: 2.7×10 kHz

Fig. 5. Result of the modal analysis

section III-B. Figure 5 illustrates deformation modes and corresponding natural frequencies of the first three modes. The first mode corresponds to the vibration in the normal, while the remaining two modes correspond to that in the tangential direction. This elastic body was confirmed to have enough rigidity, over 4.7 kHz natural frequency, to measure voluntary human movement or static load in human function studies.

IV. PERFORMANCE

A. Calibration

Since we are designing a uniaxial force sensor, we only use one axial (x axial) sensibility of the micrometry given in section II. Displacement of the encoder lens dx in the normal direction is proportional to the applied force f in the same direction when the deformation of the elastic body is minute. We thus obtain an equation which relate the applied force and the resulting differential voltages as

$$f = c' \frac{1}{2} c \mathbf{r} [dV_{\xi}, dV_{\psi}]^T = c'' dV_{\xi}, \quad (5)$$

where c' and $c'' = c'/2$ are the proportionality constants, while $\mathbf{r} = [1, 0]$ is the first row of the rotation matrix \mathbf{R} (we

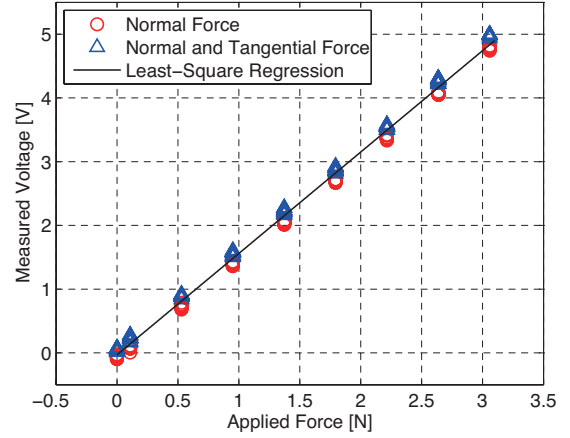


Fig. 6. Output voltage against applied force and result of least-square approximation for computing calibration coefficient

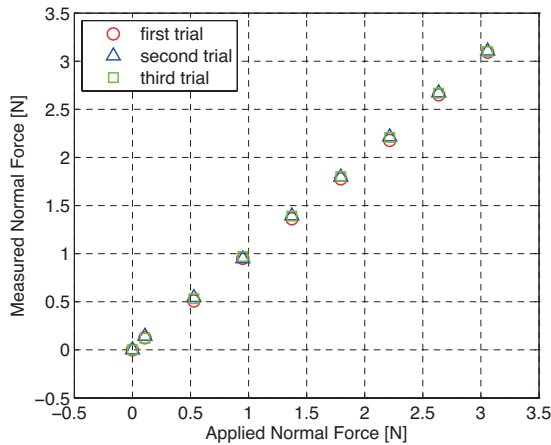
assume it to be an identity matrix in this case) given in equation (4). The unknown constant c'' in equation (5) was estimated by a least square method using training data, sets of known applied force and resulting differential voltage. The accuracy of the force sensor is then evaluated by validation data, set of known applied force and resulting differential voltage that do not used for the estimation of the constant c'' .

Figure 6 shows measured differential voltage against applied force. There are two conditions in the test force: application of the normal force (red circle), and application of both the normal and the tangential force with the same quantity (blue triangle). Both conditions have ten trials. As can be seen in this plot, the obtained differential voltage have linear relationship with the applied force. This suggests that the developed force sensor has little hysteresis and high axial independence. We have estimated the slope of this relationship by using linear regression to compute the applied force from the differential voltage.

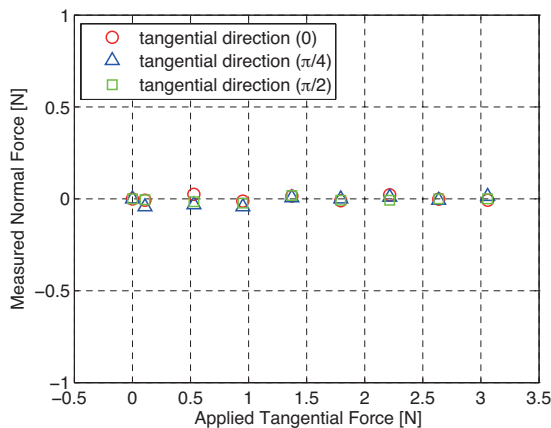
B. Accuracy

Figure 7-(a) shows the result of the first evaluation: relation between the applied normal force and the measured normal force. In order to evaluate the hysteresis characteristics and the reproducibility, the normal force was applied to the sensor head three times repeatedly. As can be seen in this plot, the measured force is almost linear and is free from hysteresis. The accuracy of the measured force was better than 1.4 % of the full scale, 3 N in the case of this force sensor.

Figure 7-(b) shows the result of the second evaluation: relation between the applied tangential force and the measured normal force. Same as section III-B, tangential force was applied in three directions 0, $\pi/4$ and $\pi/2$ radian with the optical axis of the encoder lens. As can be seen in this plot, the applied tangential force have little influence on the measured normal force. The error of the measured normal force was at most 1.6 % of the full scale.



(a) Measured normal force against applied normal force



(b) Measured normal force against applied tangential force

Fig. 7. Accuracy of the force sensor

The accuracy of the force sensor including hysteresis characteristics and axial interference was confirmed to be 1.6 % of the full scale. It is about twice as good as Tada and Kanade’s implementation [11] thanks to the parallel plate structure.

C. MRI Compatibility

We evaluated the MRI compatibility of a force sensor [11] that is made of the same material and has similar dimensions. The inhomogeneity of the magnetic field (IMF) and the loss of the signal-to-noise ratio (SNR) of the obtained images caused by the insertion of the force sensor into MRI scanner were the inspection items in this evaluation.

The evaluation revealed that the force sensor has little influence on MRI: the inhomogeneity of the magnetic field is estimated to be 0.49 ppm, while the loss of signal-to-noise ratio of the obtained image is less than 8% even though the sensor is placed at the center of the MRI bore. Please refer to [11] for the detail of this evaluation.

D. Discussion

Table III shows the specifications of the developed force sensor. The sensor head component has parallel plate struc-

TABLE III
SPECIFICATIONS OF THE DEVELOPED FORCE SENSOR

Name	Value
Dimension	diameter: 25 mm, height: 11 mm
Weight	6.5 g (without optical fibers)
Material	glass fiber reinforced PEEK polyacetal resin
Fiber length	10 m
Rated force	3.0 N
Accuracy	1.6 %F.S. (with hysteresis and interference)
Rigidity	2.1×10^{-1} N/ μ m

ture and is made of glass fiber reinforced PEEK those help to reduce axial interference and hysteresis characteristics of plastic resin. Our sensor is small and light, and has optical fibers with 10 meters long. The natural frequency is large enough to measure voluntary human movement (4.7 kHz). Thus it satisfies every request of force measurement inside MRI scanner room. We have confirmed that the accuracy and the rigidity of the developed force sensor are comparable to those of the commercially available force sensors.

V. CONCLUSION

In this paper, we have presented an MRI-compatible optical force sensor: its principle, structure and performance. The accuracy of this force sensor was better than 1.6 % of the full scale including hysteresis and axial interference. Since our sensor has small dimension (25 mm in diameter and 11 mm in height), light weight (6.5 g) and long optical fibers (10 m), it satisfies every request of force measurement inside MRI scanner room. We expect that this sensor is utilized in human studies in the area of biomechanics, brain function and MRI-guided surgery, that require accurate and reliable force measurement inside MRI.

REFERENCES

- [1] Kiyoyuki Chinzei, Ron Kikinis, and Ferenc A. Jolesz. MR compatibility of mechatronic devices: Design criteria. In *Proceedings of the Second International Conference on Medical Image Computing and Computer Assisted Intervention*, pages 1020–1030, 1999.
- [2] Marc Petre, Ahmet Erdemir, and Peter R. Cavanagh. An MRI-compatible foot-loading device for assessment of internal tissue deformation. *Journal of Biomechanics*, 41(2):470–474, 2008.
- [3] H. Henrik Ehrsson, Anders Fagergren, Tomas Jonsson, Göran Westling, Roland S. Johansson, and Hans Forssberg. Cortical activity in precision- versus power-grip tasks: An fMRI study. *Journal of Neurophysiology*, 83(1):528–536, 2000.
- [4] Christopher P. Cheng, Douglas F. Schwandt, Eric L. Topp, James H. Anderson, Robert J Herfkens, and Charles A Taylor. Dynamic exercise imaging with and MR-compatible stationary cycle within the general electric open magned. *Magnetic Resonance in Medicine*, 49:581–585, 2003.
- [5] Ken Masamune, Etsuko Kobayashi, Yoshitaka Masutani, Makoto Suzuki, Takeyoshi Dohi, Hiroshi Iseki, and Kintomo Takakura. Development of an MRI-compatible needle insertion manipulator for stereotactic neurosurgery. *Journal of Image Guided Surgery*, 1:242–248, 1995.
- [6] A. Krieger, R. C. Susil, G. Fichtinger, E. Atalar, and L. L. Whitcomb. Design of a novel MRI compatible manipulator for image guided prostate intervention. In *Proceedings of the 2004 IEEE International Conference on Robotics and Automation*, pages 377–382, 2004.

- [7] J. Z. Liu, T. H. Dai, T. H. Elster, V. Sahgal, R. W. Brown, and G. H. Yue. Simultaneous measurement of human joint force, surface electromyograms, and functional MRI-measured brain activation. *Journal of Neurosciece Methods*, 101:49–57, 2000.
- [8] D. Chapuis, R. Gassert, L. Sacher, E. Burdet, and H. Bleuler. Design of a simple MRI/fMRI compatible force/torque sensor. In *Proceedings of 2004 IEEE/RSJ International Conference on Intelligent Robots and Systems*, pages 2593–2599, 2004.
- [9] Mitsunori Tada and Takeo Kanade. An MR-compatible optical force sensor for human function modeling. In *Proceedings of the International Conference on Medical Image Computing and Computer Assisted Intervention*, pages 129–136, 2004.
- [10] Joseph Hidler, Timea Hodics, Benjamin Xu, Bruce Dobkin, and Leonardo G. Cohen. MR compatible force sensing system for real-time monitoring of wrist moments during fMRI testing. *Journal of Neurosciece Methods*, 155:300–307, 2006.
- [11] Mitsunori Tada and Takeo Kanade. Design of an MR-compatible three-axis force sensor. In *Proceedings of the IEEE/RSJ International Conference on Intelligent Robots and Systems*, pages 2618–2623, 2005.